

Article

Numerical Investigation of Heat Transfer and Flow Characteristics of Supercritical CO₂ in Solar Tower Microchannel Receivers at High Temperature

Xiaoru Zhuang ¹, Haitao Wang ¹, Haoran Lu ², Zhi Yang ^{3,*} and Hao Guo ^{4,*}

¹ School of Mechanical and Electrical Engineering, Shenzhen Polytechnic University, Shenzhen 518055, China; zhuangxr@szpt.edu.cn (X.Z.); wanghaitao@szpt.edu.cn (H.W.)

² China Academy of Launch Vehicle Technology, Beijing 100076, China; lusas2002@sina.com

³ School of Material and Energy, Guangdong University of Technology, Guangzhou 510006, China

⁴ Key Laboratory of Cryogenics, Technical Institute of Physics and Chemistry, Chinese Academy of Sciences, Beijing 100190, China

* Correspondence: yangzhi@gdut.edu.cn (Z.Y.); hguo@mail.ipc.ac.cn (H.G.)

Abstract: Using supercritical CO₂ as a heat transfer fluid in microchannel receivers is a promising alternative for tower concentrating solar power plants. In this paper, the heat transfer and flow characteristics of supercritical CO₂ in microchannels at high temperature are investigated by numerical simulations. The effects of microchannel structure, mass flow rate, heat flux, pressure, inlet temperature and radiation are analyzed and discussed. The results show that higher mass flow rate obtains poorer heat transfer performance with larger flow resistance of supercritical CO₂ in microchannels at high temperature. The fluid and wall temperatures, average heat transfer coefficient and pressure drop all increase nearly linearly with the increases in heat flux and inlet temperature in the high-temperature region. Moreover, high pressure contributes to great hydraulic performance with approximate thermal performance. The effect of radiation on thermal performance is more pronounced than that on hydraulic performance. Furthermore, the optimized structures of inlet and outlet headers, as well as those of the multichannel in the microchannels, are proposed to obtain good temperature uniformity in the microchannels with relatively low pressure drop. The results given in the current study can be conducive to the design and application of microchannel receivers with supercritical CO₂ as a heat transfer fluid in the third generation of concentrating solar power plants.

Keywords: supercritical CO₂; heat transfer; microchannel; solar receiver; numerical simulation; concentrating solar power



Citation: Zhuang, X.; Wang, H.; Lu, H.; Yang, Z.; Guo, H. Numerical Investigation of Heat Transfer and Flow Characteristics of Supercritical CO₂ in Solar Tower Microchannel Receivers at High Temperature. *Energies* **2023**, *16*, 6445. <https://doi.org/10.3390/en16186445>

Academic Editor: Antonio C.M. Sousa

Received: 8 August 2023

Revised: 2 September 2023

Accepted: 4 September 2023

Published: 6 September 2023



Copyright: © 2023 by the authors. Licensee MDPI, Basel, Switzerland. This article is an open access article distributed under the terms and conditions of the Creative Commons Attribution (CC BY) license (<https://creativecommons.org/licenses/by/4.0/>).

1. Introduction

With the growing serious environmental issues, the high-efficiency utilization of solar energy has become a promising choice to solve the problems [1–3]. Concentrating solar power (CSP) technology generates electricity by transforming solar radiation into heat and nearly produces no greenhouse gas emissions. In addition, compared to photovoltaic (PV) cells, the CSP systems can deliver uninterrupted electricity regardless of the weather conditions by integrating with thermal energy storage (TES) units. Among different types of CSP technologies, the solar power tower technology can achieve higher operation temperature when compared to the parabolic trough and linear Fresnel technologies. This higher temperature yields greater thermal-to-electric conversion efficiency in the power block and results in lower costs for TES [4].

In a tower CSP plant, the receiver is a crucial component since the overall thermal efficiency of a CSP plant highly depends on it [5,6]. The concentrated solar radiation is absorbed by the receiver and transmitted to a heat transfer fluid (HTF). According to the CSP Gen3 demonstration roadmap proposed by the National Renewable Energy

Laboratory (NREL) [4], the supercritical CO₂ Brayton-cycle is recommended to replace the steam-Rankine cycle used in energy conversion systems of CSP plants, which could increase the energy conversion efficiency. To achieve this goal, the outlet temperature of the receiver needs to be higher than 973 K, which is not applicable to the liquid HTFs, such as synthetic oils and molten salts used in current CSP plants. Compared with the liquid HTFs, gaseous HTFs can be used at much higher operation temperature. Figure 1 shows a conceptual design of a gaseous receiver system with a modular phase change material (PCM) thermal storage system of a tower CSP plant [4]. The gaseous HTF is circulated through a receiver and heated to the sufficient temperature of the target above 973 K. Then, the hot HTF is transported down the tower to the TES system. After charging the storage, the cooled HTF is again circulated through the receiver. Power generation is decoupled from thermal energy collection by the TES system.

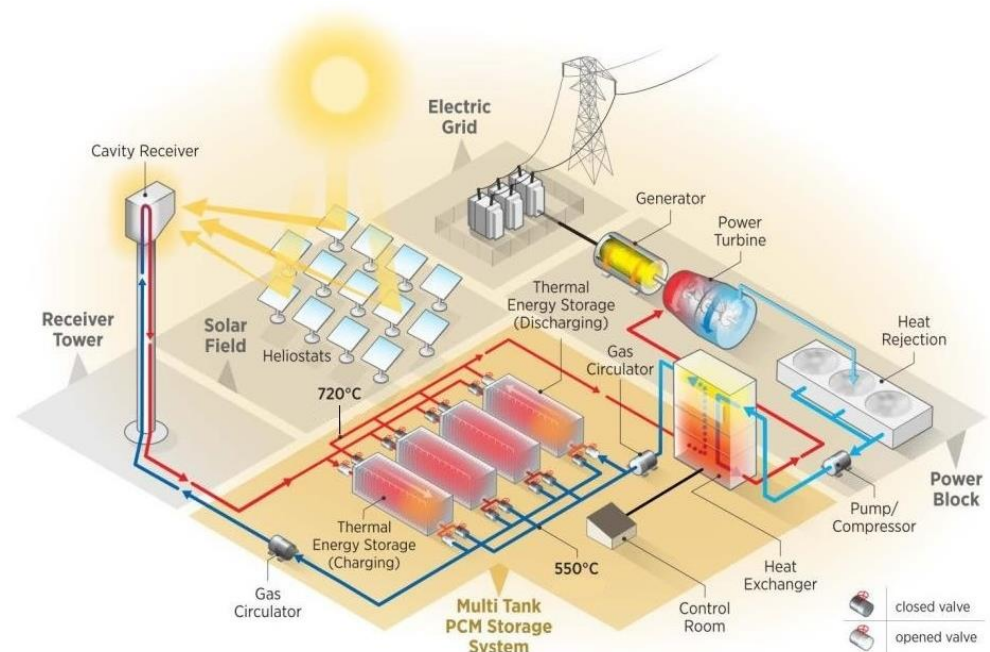


Figure 1. Conceptual design of a gaseous receiver system with a modular PCM thermal storage system of a tower CSP plant [4].

CO₂ is an attractive fluid that can be used not only in the energy conversion systems but also as a gaseous HTF in the receivers of CSP plants. It has high thermal storage capacity with much lower critical pressure and temperature (7.38 MPa and 304.25 K), which is easy to attain the critical state [7]. Moreover, CO₂ is non-flammable, non-toxic, abundant at a reasonable cost and environmentally friendly. In recent years, a considerable amount of research has been performed on the heat transfer and flow characteristics of supercritical CO₂ in the heat exchangers for CSP systems, employing both numerical and experimental approaches. Khalesi and Sarunac [8] conducted a numerical analysis of thermal and hydraulic performance of supercritical CO₂ and liquid sodium in a rectangular microchannel heat exchanger. Supercritical CO₂ was the absorbing heat fluid at the cold side with a temperature range of 300–370 K and a pressure range of 8–30 MPa. It was found that variations in the thermophysical properties of supercritical CO₂ in the critical and pseudo-critical regions had a large effect on the pressure drop and heat transfer coefficient. However, the influences of the operating conditions (pressure and inlet temperature) diminished further away from the critical point. Liu et al. [9] numerically investigated the heat transfer characteristics of supercritical CO₂ in the straight circular pipe and printed circuit heat exchanger (PCHE) components at a temperature range of 260–400 K and a pressure range of 8–20 MPa. The results presented that high heat flux and low mass flow rate were

more likely to cause supercritical CO₂ heat transfer deterioration. And the heat transfer deterioration effect was enhanced when supercritical CO₂ was in the gas-like region, while the heat transfer enhancement effect was more significant when supercritical CO₂ was in the liquid-like region. Pidaparti et al. [10] experimentally studied the flow and heat transfer characteristics of supercritical CO₂ in the PCHEs with discontinuous offset rectangular and airfoil fins at a temperature range of 293~473 K and a pressure range of 7.5~10.2 MPa. The results show that the heat transfer coefficient peaked near the pseudo-critical temperature due to the increased specific heat in the pseudo-critical region. However, the magnitude of the peak decreased with the increase in operating pressure. When the fluid temperatures were greater than the pseudo-critical temperature, the heat transfer coefficients were higher for the higher operating pressures, and the pressure drops were much higher due to the larger fluid velocities. Similar conclusions were also obtained by Zhang et al. [11], who conducted an experimental investigation of the thermal phenomenon of supercritical CO₂ heated in horizontal rectangular microchannels. The operating conditions were in the temperature range of 290~440 K and a pressure range of 9~12 MPa. It was also found that the buoyancy had a smaller effect on heat transfer in the 1 mm diameter channel than in the 2 mm diameter channel. Wang et al. [12] performed a 3D fin shape optimization for the PCHE to improve the thermal-hydraulic performance compared against conventional cylindrical and airfoil fins. The optimized 3D fins featured variable cross-sections along the height direction. Supercritical CO₂ was both the cold and hot sides' fluid with a temperature range of 318.15~678.15 K and a pressure range of 7.5~26 MPa. The numerical results presented that these 3D fins significantly reduced the impact area of fluid, which was conducive to reduce the local flow resistance caused by the high-velocity gradient and consequently improve the comprehensive thermal performance. Shi et al. [2] numerically investigated the thermal and hydraulic performance of supercritical CO₂ and molten salt in the PCHEs. Supercritical CO₂ was in the high temperature range of 779~1073 K with a constant pressure of 20 MPa. Three channel structures of straight, zigzag and airfoil were compared. The results indicate that the distributed airfoil fins could enhance the disturbance and achieve better thermal performance without exceeding the increment of the flow friction. Moreover, the larger inlet temperature caused a lower heat transfer coefficient of supercritical CO₂. And the friction factor decreased with the increment of the inlet temperature.

Reviewing the literature, it was found that most of the investigated temperatures in heat exchangers are far lower than the temperature in solar tower receivers for the third generation of CSPs. It is known that the thermal and hydraulic performance of supercritical CO₂ is directly influenced by the thermophysical properties, which vary significantly with the temperature. However, only a few studies have focused on the utilization of supercritical CO₂ in solar tower receivers at present. Roldán and Fernández-Reche [13] made a preliminary analysis of a tubular receiver with supercritical CO₂ as an HTF in solar towers using a simplified CFD model. The results show that the heat gained by supercritical CO₂ was approximately 75% greater than that captured by molten salts at the same inlet temperature of 715 K with a pressure range of 7.5~9.7 MPa. They indicated that, considering the required operating conditions and the maintenance cost, the use of supercritical CO₂ as an HTF in solar tower receivers seemed to be a promising alternative. Overall, supercritical CO₂ requires high pressure; thus a tubular receiver is operated only when using high-thick tubes. However, when a thicker tube is used, the cost increases and thermal efficiency decreases [14]. Therefore, it seems more appropriate to use the microchannel for solar tower receivers. Bessarati et al. [15] used a mathematical model for parametric geometrical analysis of multilayer, microchannel heat sinks using supercritical CO₂ for solar tower receivers. The receiver heated supercritical CO₂ with a mass flow rate of 1 kg s⁻¹ from 803.15 K to 973.15 K at a solar flux density of 500 kW m⁻². The geometrical variables were hydraulic diameter, number of layers and distance between the channels. The results demonstrate that the increase in hydraulic diameter slightly raised the thermal resistance. The same trend occurred when increasing the number of layers from three to

eight. Moreover, the thermal resistance was independent of the distance between each channel, whereas an increase in this parameter increased the pressure drop. Wang et al. [16] conducted a numerical study of the convective heat transfer characteristics of supercritical CO₂ in mini-channels under unilateral heating conditions for the design and optimization of the compact solar receiver. The operating conditions were at the inlet temperatures of 423.15 K and 673.15 K and pressures of 9 MPa and 20 MPa. The results presented that the average heat transfer coefficient under the unilateral heating condition was slightly lower than that under the bilateral heating condition. However, for the local heat transfer, the unilateral heating condition had an adverse effect on the convective heat transfer on the heated side by reducing the turbulent kinetic energy and increasing the dynamic viscosity, which was opposite on the unheated side. Moreover, the buoyancy and thermal acceleration effects were weakened as the inlet velocity increased in both downward and upward flows, and they were strengthened due to the increased heat flux. Oregon State University [17,18] developed the microchannel solar tower receivers for supercritical CO₂ using an array of modular microchannel cells. Two structural unit cells of a parallel microchannel design and a microscale pin fin array design were fabricated in 2 cm × 2 cm, and the experiments were conducted. The results indicate that using the microchannel receiver had the ability to absorb heat flux up to 1000 kW m⁻² with a thermal efficiency exceeding 90% and an exit fluid temperature of 923 K. Furthermore, a network-type mathematical model was used to simulate the performance of multiple unit cells and full-scale receivers accounting for the multimode effect of heat transfer in a single unit cell. The results show that the modular design has the advantage of controlling the flow rate in each unit, which could accommodate the varying heat flux levels of the solar tower and ensure a prescribed outlet temperature to achieve consistent efficiency.

It is evident from the preceding literature review that the use of supercritical CO₂ as an HTF in microchannel receivers is a promising alternative for tower CSP plants. A thorough understanding of heat transfer and flow characteristics of supercritical CO₂ at high temperature (above 823 K) is the basis for its application. In addition, due to the high temperature, the radiative heat transfer generally plays an important role in solar tower receivers. Khivisara et al. [19] performed a 2D numerical study to characterize the effect of radiated heat transfer on thermal performance of supercritical CO₂ in a circular tube at the inlet temperature of 650 K, pressure of 10 MPa and uniform wall heat flux of 5–10 kW m⁻² for CSP plants. It was found that large errors in the prediction of the wall temperature and, by extension, the component lifetime could be encountered if radiation was not accounted for in heat transfer calculations. Moreover, the effect of radiation was expected to be significant at high values of wall heat fluxes. Therefore, the present work focuses on evaluating the heat transfer and flow characteristics of supercritical CO₂ in the microchannels at high temperature. The influences of mass flow rate, heat flux, pressure and inlet temperature were numerically investigated over the range of 0.2–1.6 g s⁻¹, 100–500 kW m⁻², 7.5–30 MPa and 723–873 K, respectively. Also, the effects of microchannel structure and radiation on thermal and hydraulic performance are discussed. The results obtained in this study can be conducive to the design and application of microchannel receivers with supercritical CO₂ as an HTF in the third generation of CSP plants.

2. Thermophysical Properties of CO₂

Figure 2 provides the thermophysical properties of CO₂ at a critical pressure of 8.5 MPa [20]. It can be seen that the properties of CO₂ change rapidly in the pseudo-critical temperature region, where the density, thermal conductivity and viscosity drop sharply, and the specific heat reaches the peak near the critical point. However, the density and specific heat show little variations in the high-temperature region. Moreover, the thermal conductivity and viscosity show opposite trends in the two temperature regions. These factors may make a difference in the heat transfer and flow characteristics of supercritical CO₂ in the two temperature regions. Figure 3 illustrates the thermophysical properties of CO₂ in the high-temperature region at different pressures from 7.5 to 30 MPa [20]. It is

shown that all properties increase as the pressure increases, while the impact is very small except for density.

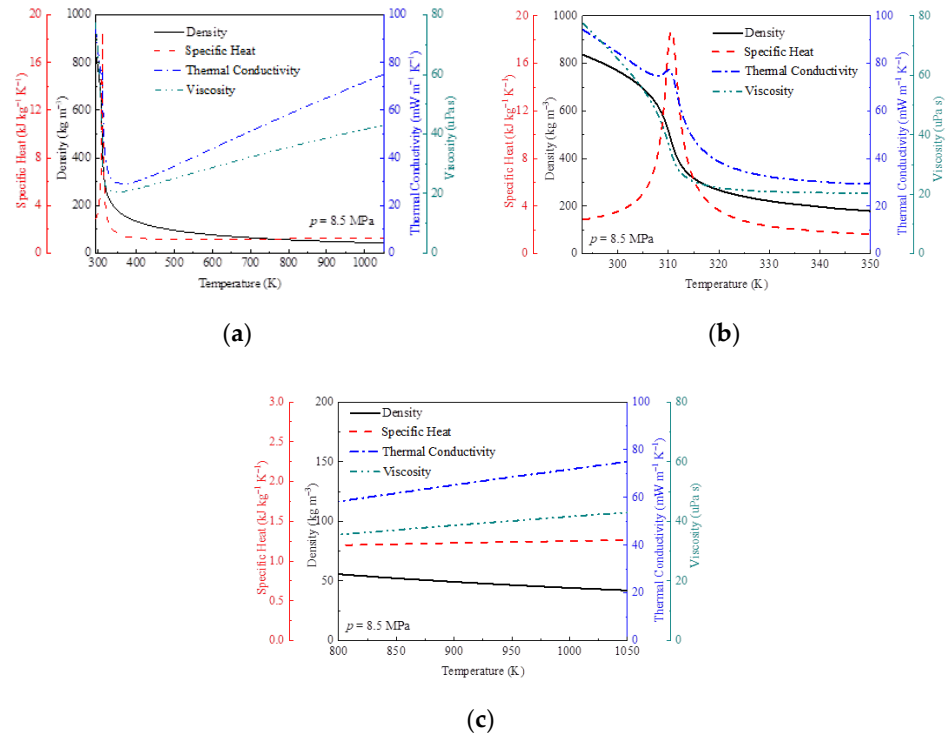


Figure 2. Properties of CO₂ at $p = 8.5$ MPa: (a) $T = 293\sim 1050$ K; (b) $T = 293\sim 350$ K; (c) $T = 800\sim 1050$ K.

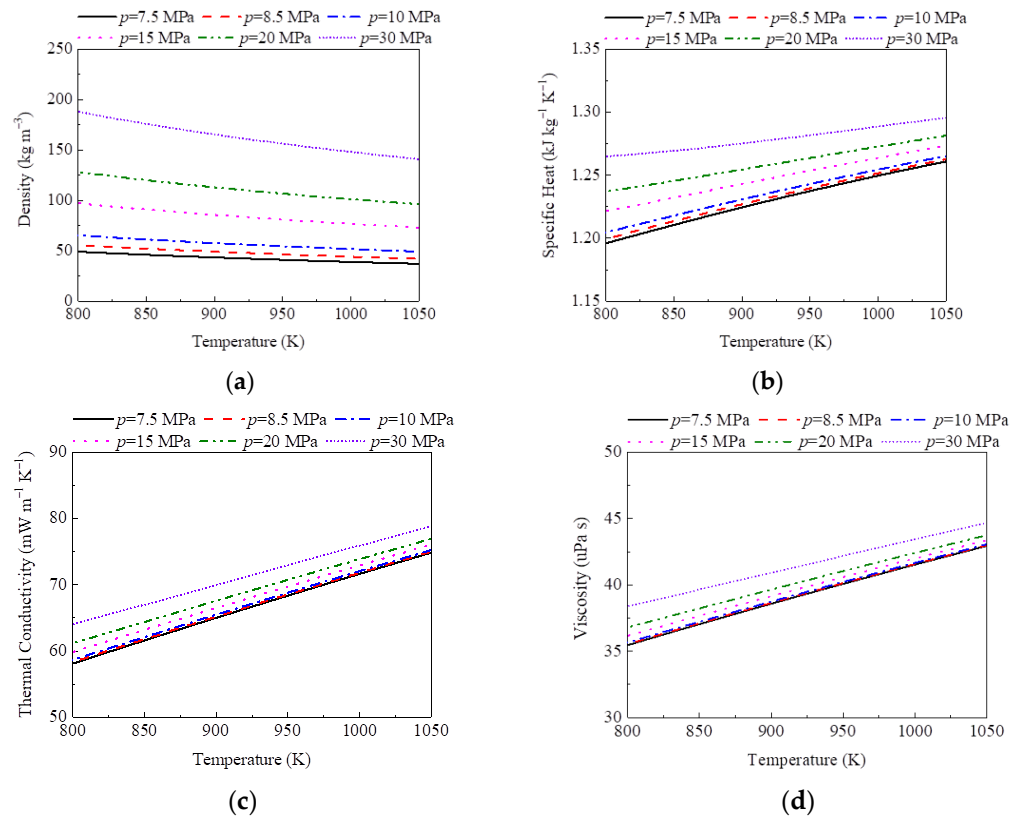


Figure 3. Properties of CO₂ in the high-temperature region of $T = 800\sim 1050$ K with $p = 7.5\sim 30$ MPa: (a) density; (b) specific heat; (c) thermal conductivity; (d) viscosity.

3. Geometry and Numerical Models

3.1. Geometry Details

The geometrical details of the microchannels used in this paper are shown in Figure 4. Both inlet and outlet headers have openings with a rectangular cross-section of 3 mm × 0.5 mm. Four header geometries with different n_H , namely H I~H IV, are used as shown in Figure 4a. Furthermore, four structures of the multichannel between inlet and outlet headers, namely MC I~MC IV, are evaluated as shown in Figure 4c. It can be seen that MC I consists of 10 parallel channels with length, width and height of 20 mm, 1 mm and 0.5 mm, respectively, for each channel by maintaining a channel spacing equivalent to 1.5 mm. MC II~MC IV are on the basis of MC I, with different intervals connecting the parallel channels.

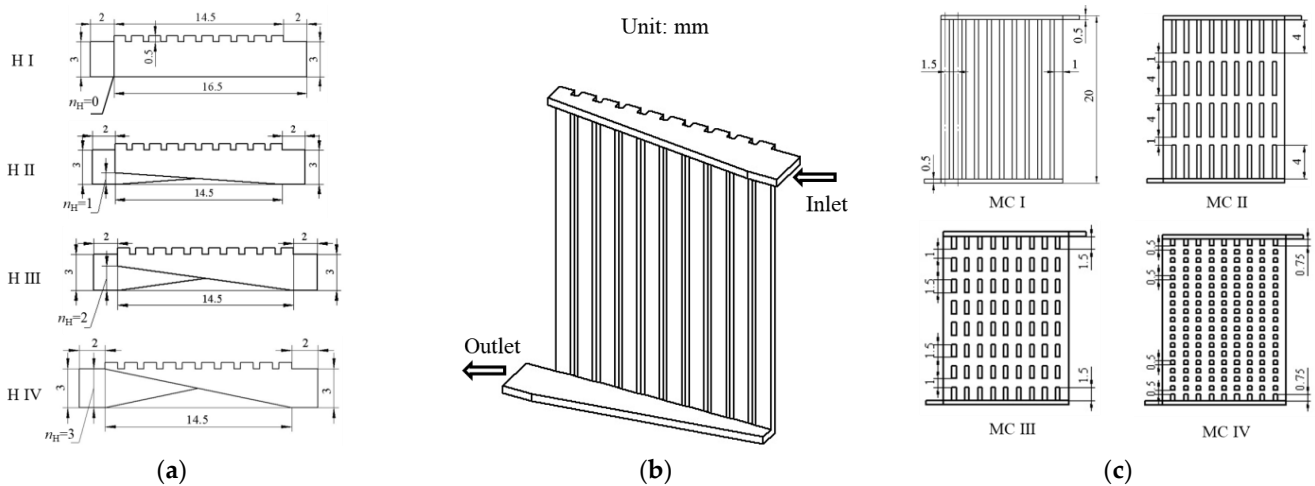


Figure 4. Geometrical details of the microchannels: (a) top view of the microchannels for H I~H IV; (b) axonometric drawing of the microchannel for H III and MC I; (c) front view of the microchannels for MC I~MC IV.

3.2. Numerical Model

In the present study, the flow is assumed to be steady and the governing equations can be described as follows:

Continuity:

$$\frac{\partial}{\partial x_i}(\rho u_i) = 0 \quad (1)$$

Momentum:

$$\frac{\partial}{\partial x_j}(\rho u_i u_j) = \rho g_i - \frac{\partial p}{\partial x_i} + \frac{\partial}{\partial x_j} \left[(\mu + \mu_t) \left(\frac{\partial u_i}{\partial x_j} + \frac{\partial u_j}{\partial x_i} - \frac{2}{3} \delta_{ij} \frac{\partial u_l}{\partial x_l} \right) \right] \quad (2)$$

Energy:

$$\frac{\partial}{\partial x_i}(\rho u_i c_p T) = \frac{\partial}{\partial x_i} \left(\lambda \frac{\partial T}{\partial x_i} \right) \quad (3)$$

where ρ is the density; u is the velocity; p is the pressure; c_p is the specific heat; T is the temperature; λ is the thermal conductivity; μ is the dynamic viscosity; μ_t is the turbulent viscosity.

A suitable turbulence model is important to the accurate predictions of the flow and heat transfer characteristics of supercritical CO₂. According to the review of the literature, the standard k - ϵ model can predict the heat transfer characteristics of supercritical CO₂ well in the high-temperature region for a parabolic trough solar collector [7]. Thus, the standard

k - ε turbulent model is adopted for simulations in this study. The transport equations for turbulent kinetic energy, k , and its rate of dissipation, ε , are defined as follows [21]:

$$\frac{\partial}{\partial x_i}(\rho u_i k) = \frac{\partial}{\partial x_j} \left[\left(\mu + \frac{\mu_t}{\sigma_k} \right) \frac{\partial k}{\partial x_j} \right] + G_k + G_b - \rho \varepsilon \quad (4)$$

$$\frac{\partial}{\partial x_i}(\rho u_i \varepsilon) = \frac{\partial}{\partial x_j} \left[\left(\mu + \frac{\mu_t}{\sigma_\varepsilon} \right) \frac{\partial \varepsilon}{\partial x_j} \right] + c_1 \frac{\varepsilon}{k} (G_k + c_3 G_b) - c_2 \rho \frac{\varepsilon^2}{k} \quad (5)$$

where

$$G_k = -\rho \frac{\partial u_j}{\partial x_i} \left(\frac{\partial u_i}{\partial x_j} + \frac{\partial u_j}{\partial x_i} \right) \quad (6)$$

$$G_b = \beta g_i \frac{\mu_t}{Pr_t} \frac{\partial T}{\partial x_i} \quad (7)$$

$$\mu_t = \frac{\rho C_\mu k^2}{\varepsilon} \quad (8)$$

where β is the thermal expansivity. The parameters of the turbulence model, σ_k , σ_ε , c_1 , c_2 , C_μ and Pr_t , are equal to 1.0, 1.3, 1.44, 1.92, 0.09 and 0.85, respectively; $c_3 = \tanh |v_2/v_1|$, and v_1 and v_2 are the components of the velocity perpendicular and parallel to the gravitational vector, respectively [7].

The boundary conditions imposed at the inlet and outlet of the computational domain are the mass flow inlet and outflow, respectively. The no-slip boundary condition is implemented on the wall of the microchannels with different heat fluxes. In order to consider the effect of radiation, the heat loss of radiation from the microchannels to the environment is calculated by [22]

$$q_{\text{rad}} = \varepsilon_{\text{rad}} \sigma_{\text{rad}} (T_w^4 - T_{\text{amb}}^4) \quad (9)$$

where ε_{rad} is the emissivity, which is 0.8; σ_{rad} is the Stefan-Boltzmann constant, which is $5.67 \text{ W m}^{-2} \text{ K}^{-4}$; T_w is the wall temperature of the microchannels; T_{amb} is the ambient temperature, which is set as a constant value of 298 K. Further details of the boundary conditions employed in this paper for the computational domain are provided in Table 1.

Table 1. List of various boundary conditions employed for the computational domain in this study.

Header	Multichannel	Inlet Temperature (K)	Pressure (MPa)	Mass Flow Rate (g s^{-1})	Wall Heat Flux without Radiation (kW m^{-2})	Wall Heat Flux with Radiation (kW m^{-2})
H I	MC I	773, 823	8.5	0.3, 1	100	--
H II	MC I	823	8.5	0.3	100	--
H III	MC I	723, 773, 823, 873	7.5, 8.5, 10, 15, 20, 30	0.2, 0.3, 0.4, 0.6, 0.8, 1.2, 1.6	100, 200, 300, 400, 500	$500 - q_{\text{rad}}$
	MC II	823	8.5	0.3	$100 A_I/A_{II}$	--
	MC III	823	8.5	0.3	$100 A_I/A_{III}$	--
	MC IV	823	8.5	0.3, 1.6	$100 A_I/A_{IV}$, $500 A_I/A_{IV}$	$500 A_I/A_{IV} - q_{\text{rad}}$
H IV	MC I	823	8.5	0.3	100	--

Note: A_I – A_{IV} are the wall areas of the microchannels for H III and different multichannels MC I–MC IV, respectively.

In this study, the commercial software Ansys-Fluent 2022 R1 is used for the numerical simulations. The equations' coupling of velocity and pressure is solved by the SIMPLEC algorithm. The QUICK scheme is employed to discretize the momentum and energy equations. Turbulence kinetic energy and turbulence dissipation rate equations are adopted with the second-order upwind scheme. The numerical calculation is considered converged when the inlet pressure, outlet and maximum wall temperatures are without observable change in the monitors, as well as when the residual error for each governing equation is less than 10^{-6} . In addition, REFPROP v9.1, provided by the National Institute of Standards

and Technology (NIST) [20], is linked to Fluent by activating the NIST real gas model to obtain accurate thermophysical properties of CO₂. The wall heat flux with radiation is integrated in CFD code through the User Defined Function (UDF).

The local and average heat transfer coefficients of the microchannels are computed numerically using the following expressions given as

$$h_{\text{loc}} = \frac{q_{\text{cf}}}{T_{\text{w}} - T_{\text{nw}}} \quad (10)$$

$$h_{\text{avg}} = \frac{1}{n} \sum_{i=1}^n h_{\text{loc},i} \quad (11)$$

where q_{cf} , T_{nw} and n are the heat flux through the cell face, near wall fluid temperature and cell number, respectively. Meanwhile, the Nusselt number is calculated as

$$Nu = \frac{h_{\text{avg}} D_{\text{h}}}{\lambda} \quad (12)$$

where D_{h} is the hydraulic diameter of the microchannels.

The pressure drop of the microchannels is calculated by

$$\Delta p = p_{\text{in}} - p_{\text{out}} \quad (13)$$

where p_{in} and p_{out} are CO₂ pressures at the inlet and outlet of the microchannels, respectively. The friction factor is expressed as

$$f = \frac{\Delta p}{L} \left(\frac{2}{\rho u^2} \right) D_{\text{h}} \quad (14)$$

where L is the length along with the flow direction; $\rho u^2/2$ is the dynamic pressure.

Performance evaluation criteria (PEC) are used to simultaneously evaluate the heat transfer and flow characteristics:

$$PEC = \frac{Nu/Nu_1}{(f/f_1)^{1/3}} \quad (15)$$

where Nu_1 and f_1 are the Nusselt number and friction factor of the microchannels for MC I, respectively.

3.3. Mesh Independence Verification and Model Validation

Poly-hexcore meshes were employed for the simulations generated by Ansys-Fluent Meshing. A grid independence test was conducted to guarantee the accuracy of computation under the conditions of inlet mass flow rate $M = 1 \text{ g s}^{-1}$, inlet temperature $T_{\text{in}} = 773 \text{ K}$, wall heat flux $q = 100 \text{ kW m}^{-2}$ and pressure $p = 8.5 \text{ MPa}$ for the microchannel with H I and MC I. Different grids with cells ranging from 2,225,750 to 5,247,454 were evaluated as presented in Table 2. It was found that the average values of y^+ are all below 1. In addition, for meshes M3 and M4, the calculated values of the outlet temperature, maximum and average wall temperatures, average heat transfer coefficient and pressure drop differ negligibly by 0.005%, 0.87%, 0.11%, 0.08% and 0.67%, respectively. At last, the mesh configuration M3 was chosen in terms of the computation accuracy and time. Figure 5 shows the finalized meshes for the computational domain.

Due to the fact that there are no available experimental data in the literature to validate the model for the heat transfer process of supercritical CO₂ in the microchannels at high temperature, the validation of the computational model was conducted indirectly using the experimental study of Kim and Kim [23], employing the same geometry (a circular tube with an inner diameter of 4.5 mm) and operating condition used for the experimental work. The comparison between the numerical and experimental results is demonstrated in

Figure 6 [24]. It is seen that the numerical results agree well with the experimental data, and the average relative errors of wall temperature and heat transfer coefficient are about 0.85% and 3.35%, respectively. Although the geometries used in the experimental study and in this paper are different, the settings of the numerical model are the same. Therefore, the numerical method employed in the present work is appropriate.

Table 2. Results of mesh independence.

Mesh	Number of Cells	Average Value of y^+	Outlet Temperature (K)	Maximum Wall Temperature (K)	Average Wall Temperature (K)	Average Heat Transfer Coefficient ($\text{W m}^{-2} \text{K}^{-1}$)	Pressure Drop (Pa)
M1	2,225,750	0.534	838.46	1310.92	891.78	709.46	12,257
M2	3,680,540	0.268	838.32	1327.97	893.31	710.99	12,323
M3	4,445,040	0.267	838.40	1330.01	892.78	711.09	11,859
M4	5,247,454	0.270	838.44	1341.64	893.74	711.65	11,939

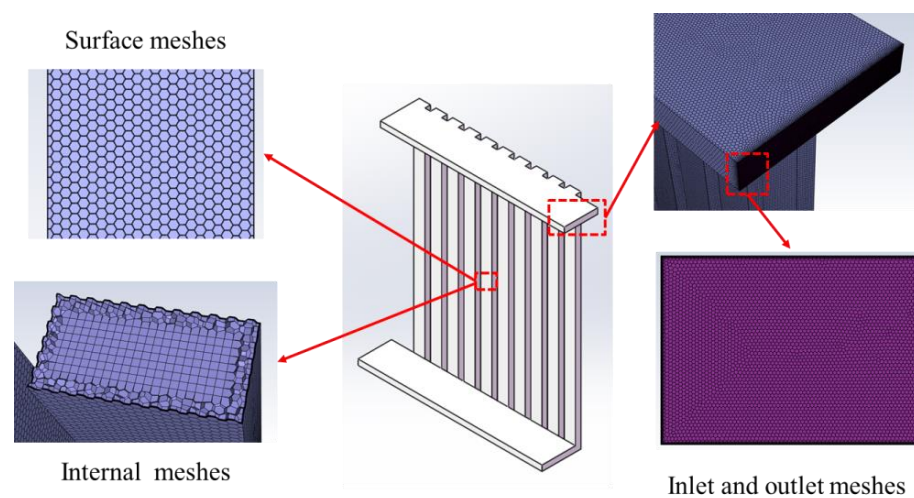


Figure 5. Exaggerated views of mesh from different locations for the microchannel with HI and MC I.

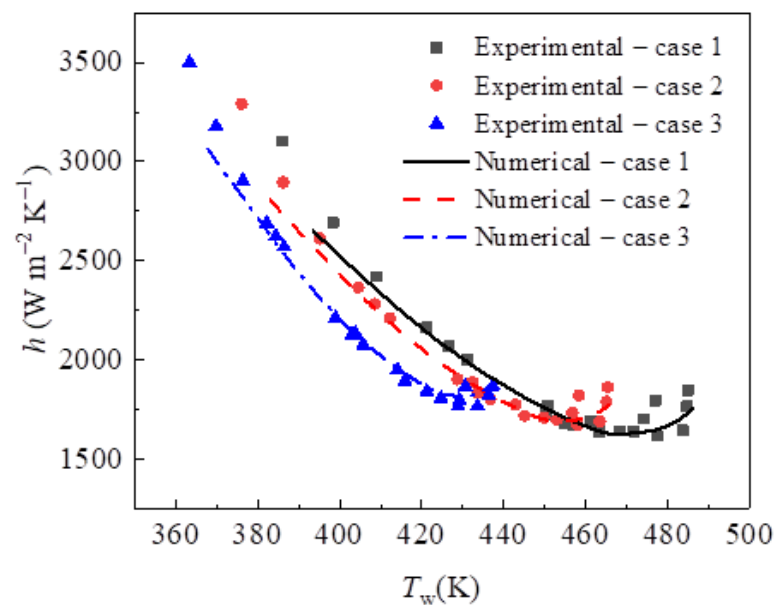


Figure 6. Comparison between numerical results and experimental data of Kim and Kim [23]. Case 1: $G = 868 \text{ kg m}^{-2} \text{ s}^{-1}$, $q = 231.0 \text{ kW m}^{-2}$, $p = 9.22 \text{ MPa}$; Case 2: $G = 873 \text{ kg m}^{-2} \text{ s}^{-1}$, $q = 216.2 \text{ kW m}^{-2}$, $p = 9.09 \text{ MPa}$; Case 3: $G = 874 \text{ kg m}^{-2} \text{ s}^{-1}$, $q = 191.8 \text{ kW m}^{-2}$, $p = 8.71 \text{ MPa}$ [24].

4. Results and Discussion

In the present study, the thermal and hydraulic performance of supercritical CO₂ as an HTF in the microchannels are evaluated in the high-temperature region. In addition, the effects of mass flow rate, heat flux, pressure, inlet temperature, microchannel structure and radiation are investigated as shown in Table 1.

In general, the inlet and outlet headers are used to distribute and collect the fluid to and from the multichannel, respectively. The geometry of the header plays a critical role in the flow distribution in the microchannel. Uniform flow distribution is conducive to obtain higher heat transfer coefficient and lower pressure drop. In this paper, four header shapes with different n_H shown in Figure 4a are compared. Figure 7 shows the wall temperature counters of the microchannels with MC I under the conditions of $M = 0.3 \text{ g s}^{-1}$, $T_{\text{in}} = 823 \text{ K}$, $q = 100 \text{ kW m}^{-2}$ and $p = 8.5 \text{ MPa}$ without radiation for different header shapes. It can be seen that there is a local high-temperature region at the end corner of the inlet header. This is prone to cause the surface cracking and thermal fatigue damage of the receiver material due to thermal stress, which is detrimental to the safe operation of tower CSP systems. Furthermore, the local high-temperature region in the inlet header gradually disappears when n_H increases. Figure 8 displays the streamlines in four inlet headers and velocity counters on the plane generated at half the height of the parallel channels of MC I corresponding to the same conditions. According to Figure 8i, a low-speed vortex appears at the end corner of the inlet header, which results in the local high temperature. When n_H increases, the vortex gradually disappears, and the fluid flowing in the inlet headers accelerates due to the smaller fluid flow area. In addition, Figure 8ii presents that the overall flow velocity in the parallel channels slightly increases with the increase of n_H , except for that of H IV. In contrast, the overall flow velocity in the parallel channels of H IV becomes lower than those of H I~H III, leading to higher wall temperature. The local high-temperature region of H IV appears at the end of parallel channels near the inlet. Table 3 provides the heat transfer and flow characteristics of supercritical CO₂ in the microchannels with MC I, corresponding to the same conditions for different n_H . It can be found that the average heat transfer coefficients are approximately equal for H I~H III, while the pressure drop rises as n_H increases. Although the average heat transfer coefficient of H IV is a little higher than those of H I~H III, the pressure drop and maximum wall temperature of H IV are both much higher than those of H III. Thus, accounting for the best temperature uniformity in the microchannel with relative low pressure drop, the inlet header of H III is used for the subsequent simulations in this study.

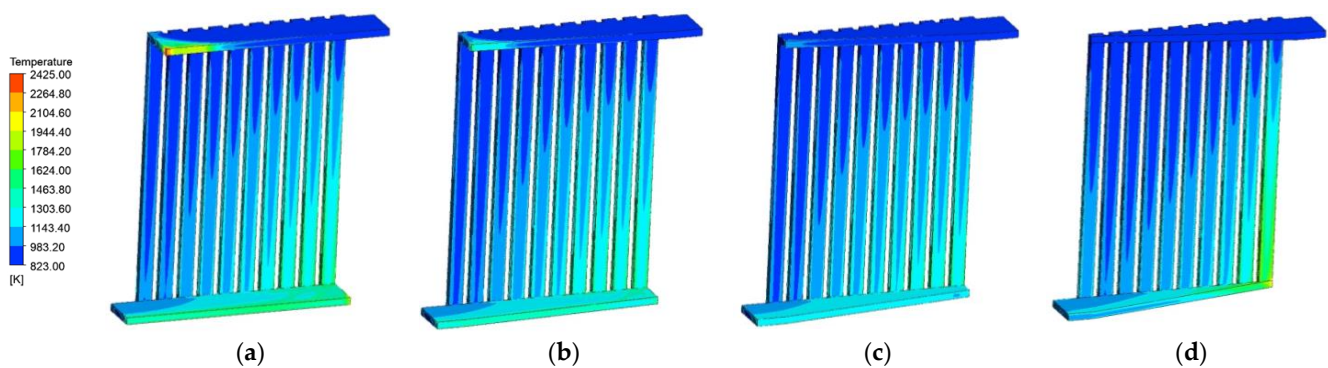


Figure 7. Wall temperature counters of the microchannels with MC I under the conditions of $M = 0.3 \text{ g s}^{-1}$, $T_{\text{in}} = 823 \text{ K}$, $q = 100 \text{ kW m}^{-2}$ and $p = 8.5 \text{ MPa}$ without radiation for (a) H I; (b) H II; (c) H III; (d) H IV.

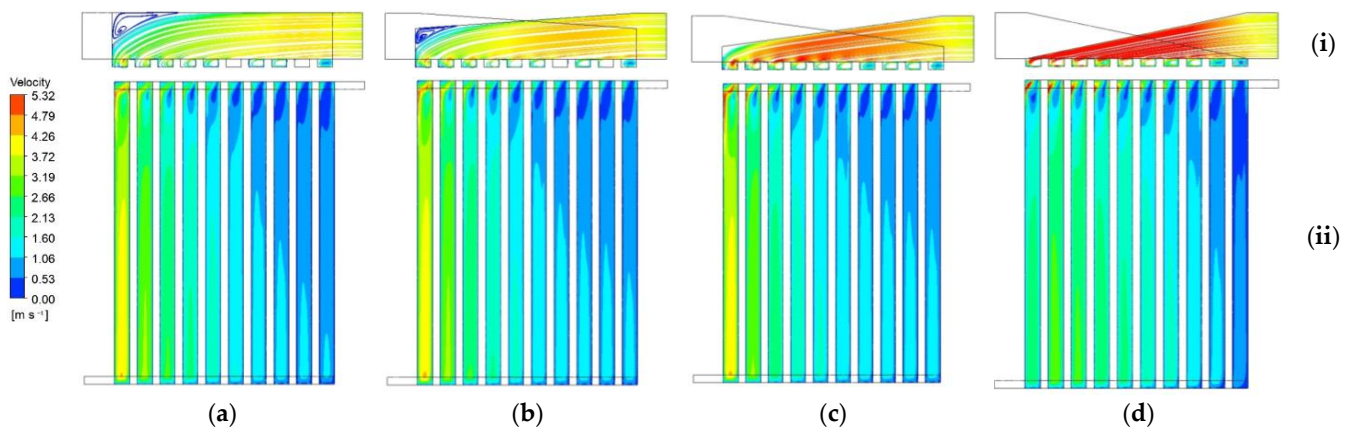


Figure 8. (i) Streamlines in the inlet header and (ii) velocity counters on the plane generated at half height of the parallel channels of MC I under the conditions of $M = 0.3 \text{ g s}^{-1}$, $T_{\text{in}} = 823 \text{ K}$, $q = 100 \text{ kW m}^{-2}$ and $p = 8.5 \text{ MPa}$ without radiation for (a) H I; (b) H II; (c) H III; (d) H IV.

Table 3. Heat transfer and flow characteristics of supercritical CO_2 in the microchannels with MC I under the conditions of $M = 0.3 \text{ g s}^{-1}$, $T_{\text{in}} = 823 \text{ K}$, $q = 100 \text{ kW m}^{-2}$ and $p = 8.5 \text{ MPa}$ without radiation for H I–H IV.

Mesh	Average Heat Transfer Coefficient ($\text{W m}^{-2} \text{ K}^{-1}$)	Pressure Drop (Pa)	Maximum Wall Temperature (K)
H I	856.57	1624	2422.78
H II	855.78	1756	1644.68
H III	856.78	1983	1584.46
H IV	867.60	2704	2219.95

Figure 9 illustrates the effect of mass flow rate on the heat transfer and flow characteristics of supercritical CO_2 in a microchannel with H III and MC I under the conditions of $M = 0.2\text{--}1.6 \text{ g s}^{-1}$, $T_{\text{in}} = 823 \text{ K}$, $q = 100 \text{ kW m}^{-2}$ and $p = 8.5 \text{ MPa}$ without radiation. It is clearly observed that the fluid and wall temperatures decrease as the mass flow rate increases, especially at lower mass flow rate. The average heat transfer coefficient is depressed, while the pressure drop is enhanced with the increase in mass flow rate. Moreover, the impact is more obvious at lower mass flow rate for the average heat transfer coefficient, and at higher mass flow rate for the pressure drop. This can be explained by the fact that the fluid velocity increases when the mass flow rate increases, which leads to the increments in flow resistance and convective heat transfer. In addition, according to Figure 3, the decreasing fluid temperature with the increasing mass flow rate also results in lower thermal conductivity and specific heat and viscosity of CO_2 . The increases in fluid velocity and viscosity both increase the pressure drop in the microchannel. Furthermore, the heat transfer enhancement due to the increasing fluid velocity may be lower than the depression due to the decreasing thermophysical properties, leading to the reduction in average heat transfer coefficient. It clarifies that the effects of thermophysical properties, such as thermal conductivity and specific heat, are more dominant on the thermal performance at high temperature. The variation of the fluid temperature is less pronounced at higher mass flow rate, and thus the effect of mass flow rate on the heat transfer coefficient becomes weaker. Moreover, the mass flow rate should be less than 0.4 g s^{-1} under this condition so that the outlet temperature can exceed 973 K to reach the target temperature of the solar tower receiver for CSP systems.

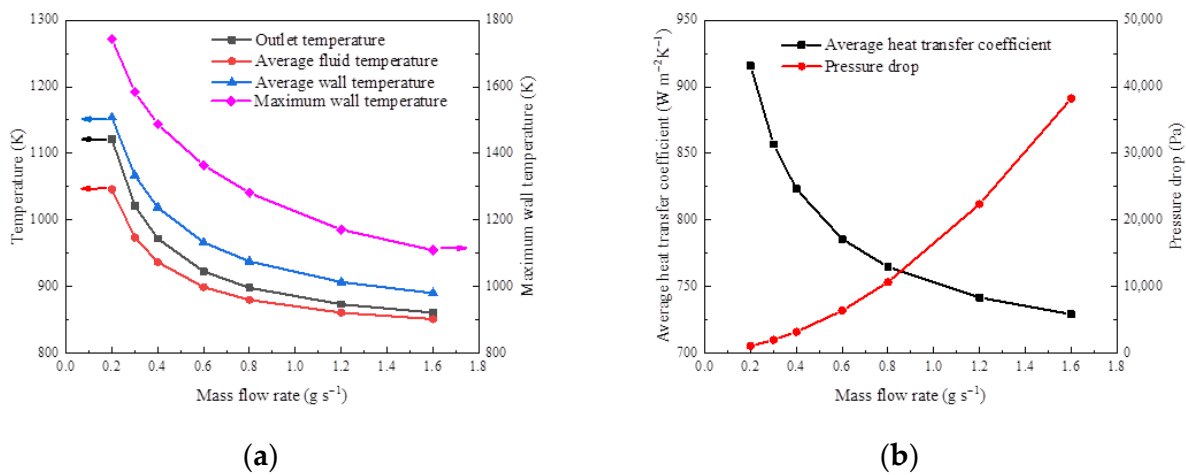


Figure 9. Effect of mass flow rate on (a) fluid and wall temperatures; (b) average heat transfer coefficient and pressure drop of supercritical CO₂ in a microchannel with H III and MC I under the conditions of $M = 0.2\sim 1.6\text{ g s}^{-1}$, $T_{in} = 823\text{ K}$, $q = 100\text{ kW m}^{-2}$ and $p = 8.5\text{ MPa}$ without radiation.

Figure 10 presents the variations in the outlet temperature, average fluid temperature, average wall temperature, maximum wall temperature, average heat transfer coefficient and pressure drop with the wall heat flux in a microchannel using H III and MC I under the conditions of $M = 1.6\text{ g s}^{-1}$, $T_{in} = 823\text{ K}$, $q = 100\sim 500\text{ kW m}^{-2}$ and $p = 8.5\text{ MPa}$ without radiation. It is shown that those parameters all increase nearly linearly with the increasing heat flux. According to Figure 3, the thermal conductivity and specific heat of CO₂ increase with the increase in temperature, which enhances the heat transfer. Moreover, the density of CO₂ decreases as the temperature increases, which can result in volume expansion, induce the flow acceleration effect at a fixed mass flow rate and increase both the heat transfer coefficient and pressure drop in the microchannel. The viscosity of CO₂ also increases with the increase in temperature, which further increases the pressure drop. Moreover, when the heat flux reaches 500 kW m^{-2} , the mass flow rate should be less than 1.6 g s^{-1} under the conditions of $T_{in} = 823\text{ K}$ and $p = 8.5\text{ MPa}$ without radiation so that the outlet temperature could be over 973 K to reach the target temperature of the solar tower receiver for CSP systems.

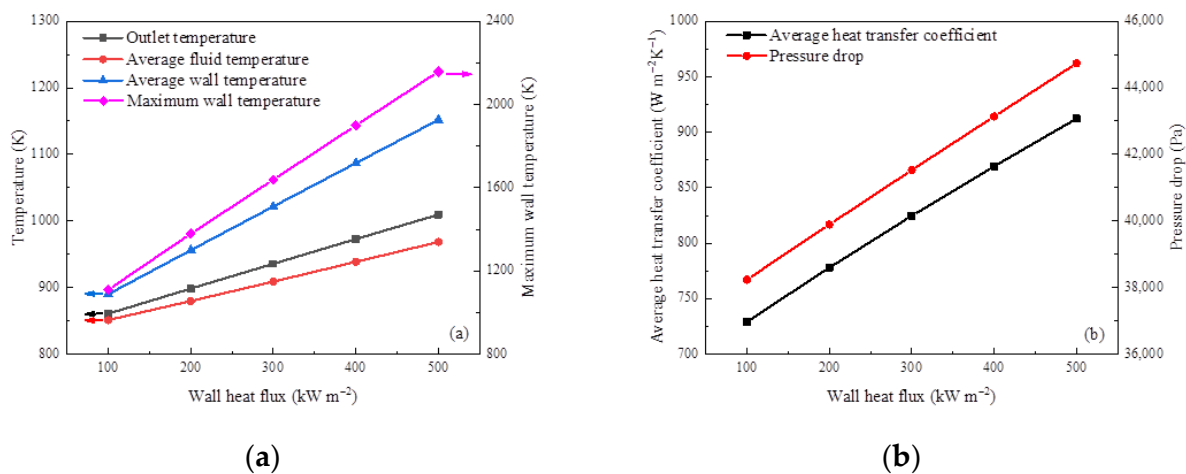


Figure 10. Effect of heat flux on (a) fluid and wall temperatures; (b) average heat transfer coefficient and pressure drop of supercritical CO₂ in a microchannel with H III and MC I under the conditions of $M = 1.6\text{ g s}^{-1}$, $T_{in} = 823\text{ K}$, $q = 100\sim 500\text{ kW m}^{-2}$ and $p = 8.5\text{ MPa}$ without radiation.

Figure 11 indicates the effect of pressure on heat transfer and flow characteristics of supercritical CO₂ in a microchannel with H III and MC I under the conditions of $M = 0.3 \text{ g s}^{-1}$, $T_{\text{in}} = 823 \text{ K}$, $q = 100 \text{ kW m}^{-2}$ and $p = 7.5\text{--}30 \text{ MPa}$ without radiation. It displays that the fluid and wall temperatures decrease slightly with the increase in pressure. The average heat transfer coefficient increases and pressure drop decreases as the pressure increases. However, the increment of the average heat transfer coefficient is only 4.62%, while the decrement of pressure drop is 73.61% when the pressure varies from 7.5 MPa to 30 MPa. It means that the variation of pressure has little influence on the thermal performance but great effect on the hydraulic performance. Although the lower fluid temperature leads to lower thermal conductivity and specific heat, as well as higher density, higher pressure also causes those thermal properties of CO₂ to become larger according to Figure 3, especially for density. The effects of the fluid temperature and pressure on the thermal conductivity and specific heat might offset each other, resulting in little change in the average heat transfer coefficient. In addition, the pressure drop rises sharply with the decreasing pressure because of the much lower density induced by lower pressure which leads to volume expansion and induces the flow acceleration effect. Moreover, higher pressure needs larger manufacturing cost for the receiver and other equipment of tower CSP plants. Despite high pressure being able to obtain great hydraulic performance of supercritical CO₂ in the microchannels at high temperature with approximate thermal performance, the choice of pressure requires comprehensive consideration.

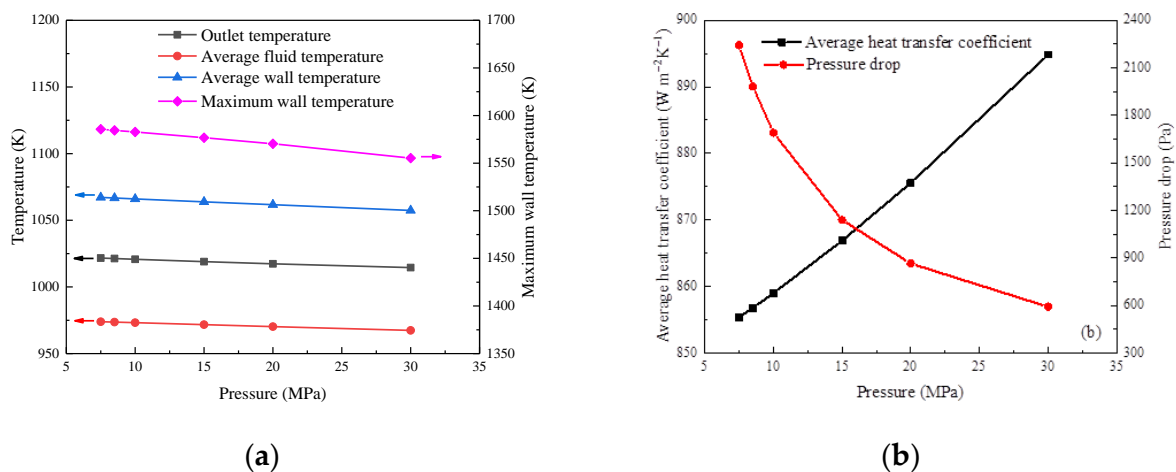


Figure 11. Effect of pressure on (a) fluid and wall temperatures; (b) average heat transfer coefficient and pressure drop of supercritical CO₂ in a microchannel with H III and MC I under the conditions of $M = 0.3 \text{ g s}^{-1}$, $T_{\text{in}} = 823 \text{ K}$, $q = 100 \text{ kW m}^{-2}$ and $p = 7.5\text{--}30 \text{ MPa}$ without radiation.

Figure 12 shows the variations in the outlet temperature, average fluid temperature, average wall temperature, maximum wall temperature, average heat transfer coefficient and pressure drop with the inlet temperature in a microchannel using H III and MC I under the conditions of $M = 0.3 \text{ g s}^{-1}$, $T_{\text{in}} = 723\text{--}873 \text{ K}$, $q = 100 \text{ kW m}^{-2}$ and $p = 8.5 \text{ MPa}$ without radiation. It can be seen that those parameters also all increase nearly linearly with the increasing inlet temperature, just like the effect of heat flux. The reasons for the enhancements of heat transfer and pressure drop are similar to the effect of heat flux. The increment of the average heat transfer coefficient is 12.32% with an increment of 18.90% for the pressure drop when the inlet temperature varies from 723 K to 873 K. It means that a higher inlet temperature can obtain better thermal performance of supercritical CO₂ in the microchannels at high temperature but poorer hydraulic performance to a similar degree.

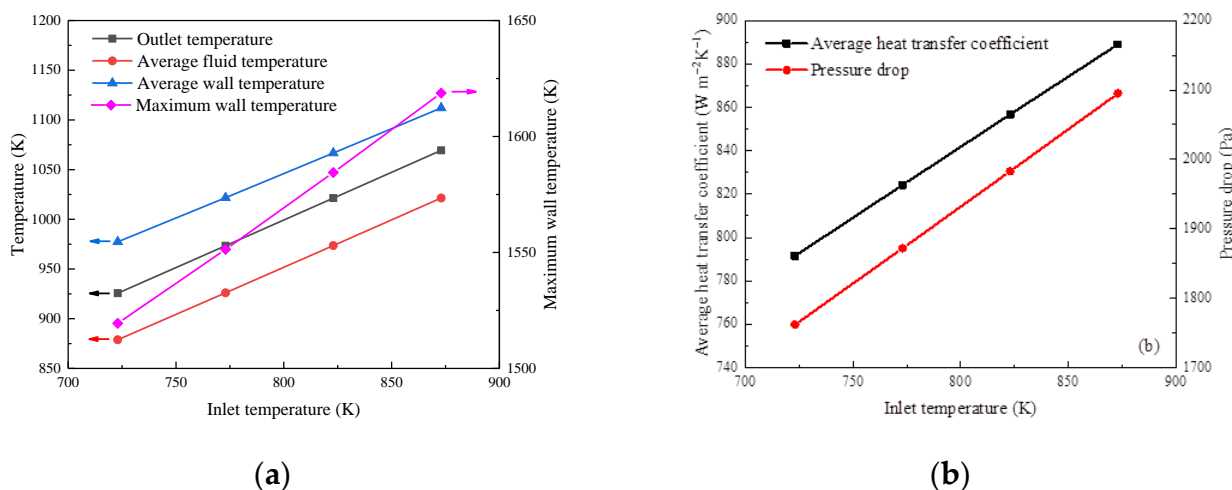


Figure 12. Effect of inlet temperature on (a) fluid and wall temperatures; (b) average heat transfer coefficient and pressure drop of supercritical CO₂ in a microchannel with H III and MC I under the conditions of $M = 0.3 \text{ g s}^{-1}$, $T_{\text{in}} = 723\text{--}873 \text{ K}$, $q = 100 \text{ kW m}^{-2}$ and $p = 8.5 \text{ MPa}$ without radiation.

In order to improve the uneven flow distribution in the microchannels, the present study proposes three more structures of multichannels (MC II~MC IV) on the basis of MC I with different intervals connecting the parallel channels, as shown in Figure 4c. Figure 13 displays the wall temperature counters of the microchannels with H III under the conditions of $M = 0.3 \text{ g s}^{-1}$, $T_{\text{in}} = 823 \text{ K}$ and $p = 8.5 \text{ MPa}$ without radiation for different multichannels. It should be noted that for the purpose of obtaining the same amount of heat, the wall heat flux is set considering the variations in area for different multichannels, as shown in Table 1. It is clearly observed that the wall temperatures of multichannels near the outlet become more uniform for MC IV than those for MC I. The local high-temperature regions are all located at the right corner of the multichannel for the four structures. The maximum wall temperatures are 1584.46 K, 1640.20 K, 1536.87 K and 1431.50 K for MC I~MC IV, respectively. It means that using the structure of MC IV in the microchannels can effectively reduce the local high temperature and obtain uniform wall temperature, which is conducive to the safe operation of the solar tower receivers. Moreover, Figure 14 presents the velocity counters on the plane generated at half height of the multichannel for MC I~MC IV corresponding to the same conditions. It is shown that the local high-velocity region is located at the left channel near the inlet for MC I, which leads to less fluid flowing through the right channel and further results in a high temperature there. However, the local high-velocity region moves to the same channel as MC I but near the outlet for MC II~MC IV. The velocity of the right channel of the multichannel significantly increases, which leads to lower local high temperature for MC IV. Table 4 compares the Nusselt number, friction factor and PEC between different structures of multichannel (MC I~MC IV) with H III, corresponding to the same conditions. It can be seen that MC I has the best thermal performance among four structures of multichannel but with a small distinction. Although MC II has the highest maximum wall temperature, its hydraulic performance is the best. MC IV is the only one whose flow resistance is higher than that of MC I. This is mainly because the overall velocity of MC IV is higher compared with MC I~MC III in Figure 14. Moreover, depending on PEC, MC I has the best thermo-hydraulic performance among four structures of multichannel, while MC III performs worst. Overall, in consideration of obvious good temperature uniformity in the microchannels with nearly equal thermo-hydraulic performance, the multichannel structure of MC IV is recommended to be used.

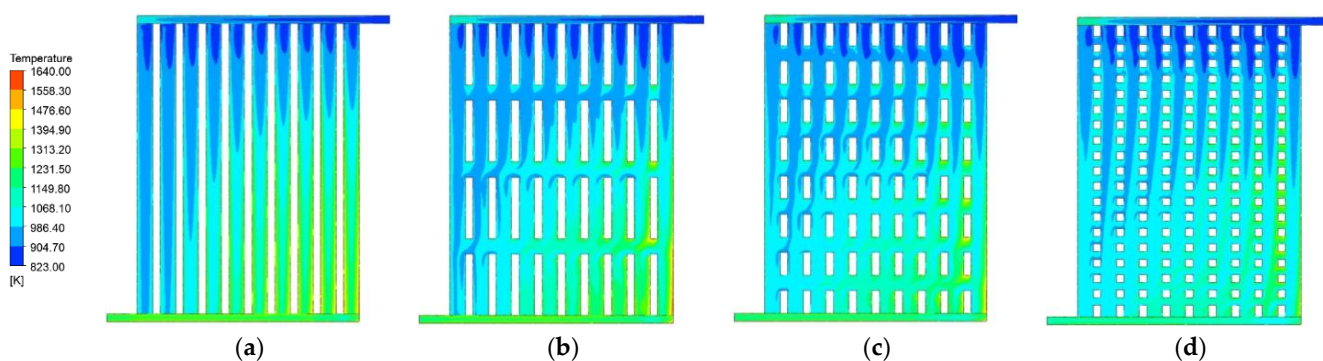


Figure 13. Wall temperature counters of the microchannels with H III under the conditions of $M = 0.3 \text{ g s}^{-1}$, $T_{\text{in}} = 823 \text{ K}$ and $p = 8.5 \text{ MPa}$ without radiation for (a) MC I; (b) MC II; (c) MC III; (d) MC IV (heat flux setting is shown in Table 1).

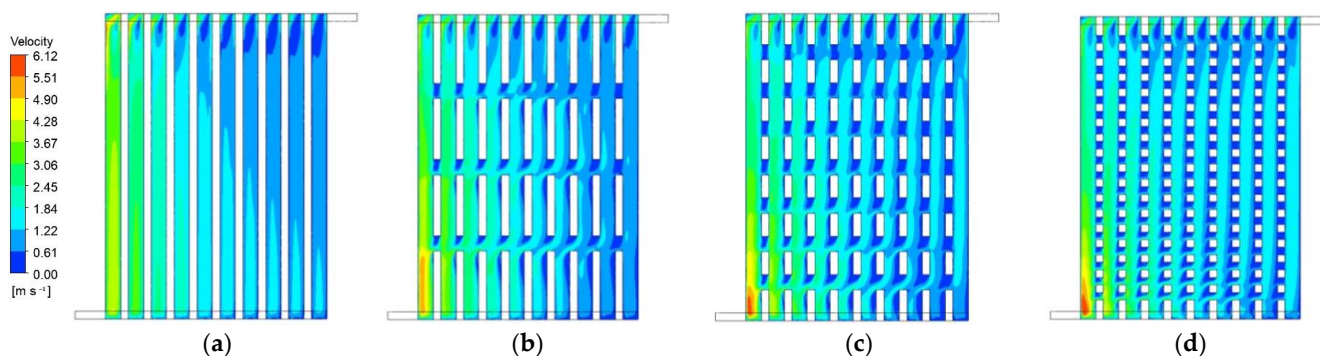


Figure 14. Velocity counters on the plane generated at half height of the multichannel of microchannels with H III under the conditions of $M = 0.3 \text{ g s}^{-1}$, $T_{\text{in}} = 823 \text{ K}$ and $p = 8.5 \text{ MPa}$ without radiation for (a) MC I; (b) MC II; (c) MC III; (d) MC IV (heat flux setting is shown in Table 1).

Table 4. Comparison of the Nusselt number, friction factor and PEC between different structures of multichannel (MC I~MC IV) with H III under the conditions of $M = 0.3 \text{ g s}^{-1}$, $T_{\text{in}} = 823 \text{ K}$ and $p = 8.5 \text{ MPa}$ without radiation (heat flux setting is shown in Table 1).

Multichannel	Nu/Nu_1	f/f_1	PEC
MC I	1	1	1
MC II	0.952	0.952	0.968
MC III	0.911	0.963	0.923
MC IV	0.938	1.001	0.937

Due to the high temperature of the solar tower receiver, radiation generally plays an important role in the thermal and hydraulic performance. Table 5 provides the heat transfer and flow characteristics of supercritical CO_2 in the microchannels with and without radiation under the conditions of $M = 1.6 \text{ g s}^{-1}$, $T_{\text{in}} = 823 \text{ K}$ and $p = 8.5 \text{ MPa}$ for MC I and MC IV, both with H III. It is shown that the effective wall heat flux becomes smaller due to radiation, which leads to lower fluid temperature, and then lower average heat transfer coefficient and pressure drop for both microchannels. Moreover, the effect of radiation on the average heat transfer coefficient and pressure drop is more obvious for MC I than that for MC IV. According to the wall temperature counters in Figure 15, the maximum wall temperatures of MC I and MC IV are reduced by 537.68 K and 259.83 K, respectively, when considering the radiation. This is because of the higher local wall temperature of MC I compared to MC IV. The radiation heat dissipations of MC I and MC IV account for 14.46% and 12.24% of the total quantity of heat, respectively. In addition, the wall temperature becomes more uniform for both microchannels when taking into account the radiation. In

terms of the velocity counters in Figure 16, the fluid velocities in multichannels slightly decrease when the radiation is taken into account, which results in a little lower pressure drop. This is due to the lower temperature with radiation than that without radiation, leading to larger density and lower viscosity. Furthermore, the effect of radiation on thermal performance is more pronounced than on the hydraulic performance of supercritical CO₂ in the microchannels at high temperature.

Table 5. Heat transfer and flow characteristics of supercritical CO₂ in the microchannels with and without radiation under the conditions of $M = 1.6 \text{ g s}^{-1}$, $T_{in} = 823 \text{ K}$ and $p = 8.5 \text{ MPa}$ for MC I and MC IV both with H III.

b	Radiation	Effective Wall Heat Flux (kW m^{-2})	Outlet Temperature (K)	Average Fluid Temperature (K)	Average Heat Transfer Coefficient ($\text{W m}^{-2} \text{K}^{-1}$)	Pressure Drop (Pa)
MC I	Without	500	1009.49	968.51	912.32	44,738
	With	427.68	983.84	944.94	876.19	43,589
MC IV	Without	452.08	1010.67	949.43	827.46	49,359
	With	396.72	988.49	934.24	807.26	48,333

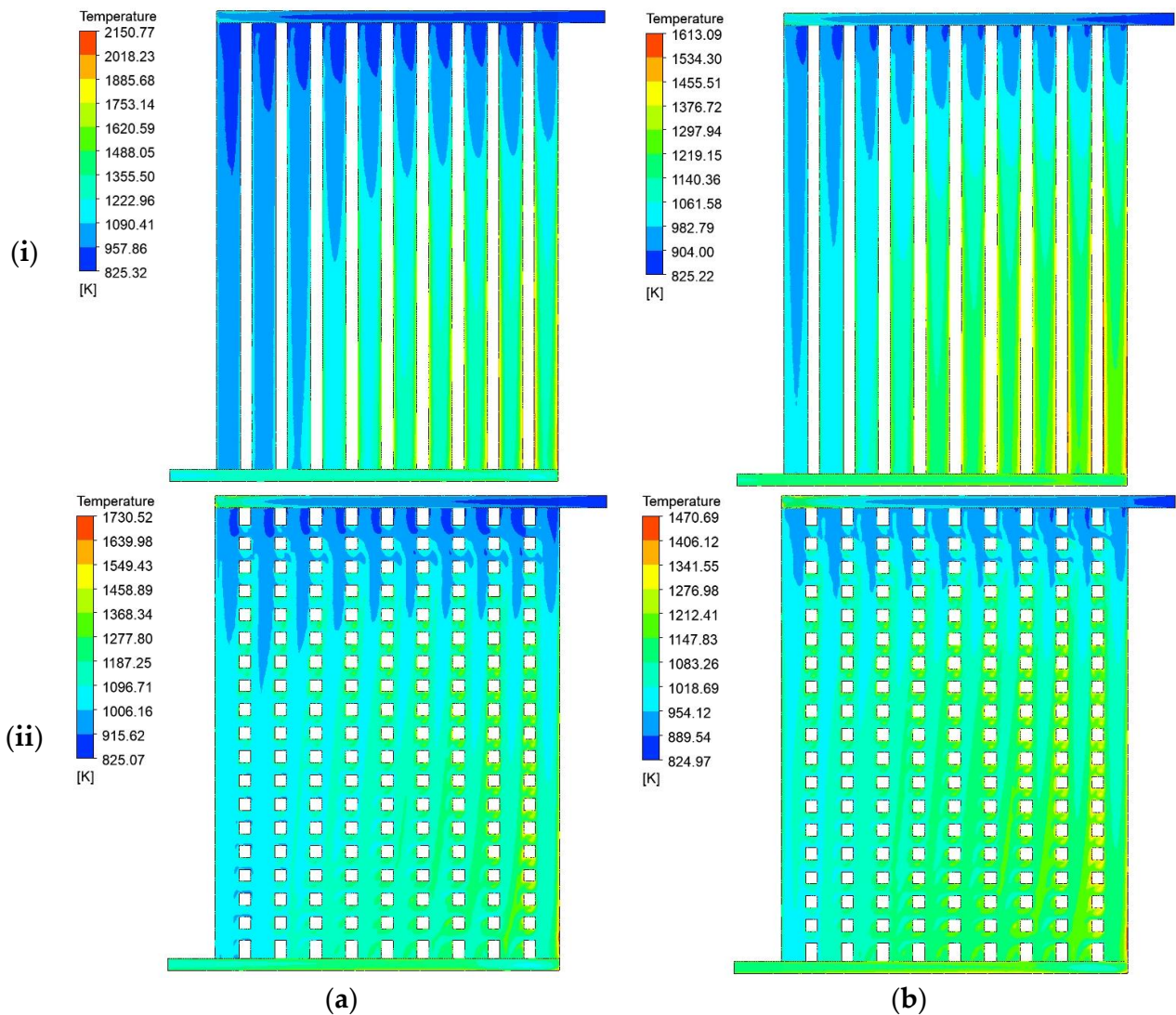


Figure 15. Wall temperature counters of the microchannels (a) without and (b) with radiation under the conditions of $M = 1.6 \text{ g s}^{-1}$, $T_{in} = 823 \text{ K}$ and $p = 8.5 \text{ MPa}$ for (i) MC I and (ii) MC IV both with H III.

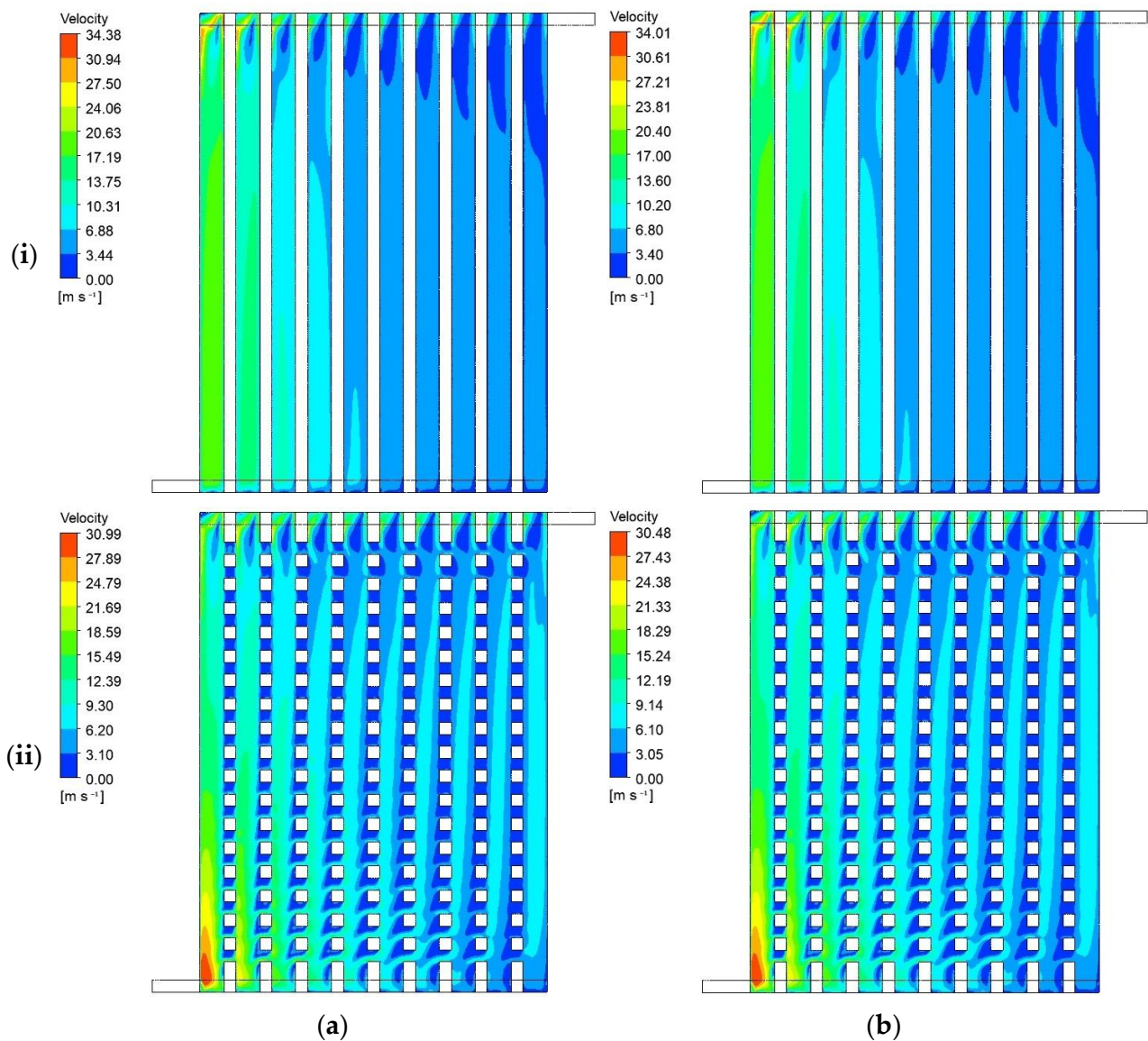


Figure 16. Velocity counters on the plane generated at half height of the multichannel of the microchannels (a) without and (b) with radiation under the conditions of $M = 1.6 \text{ g s}^{-1}$, $T_{\text{in}} = 823 \text{ K}$ and $p = 8.5 \text{ MPa}$ for (i) MC I and (ii) MC IV both with H III.

5. Conclusions

The utilization of microchannel receivers with supercritical CO_2 as an HTF is one of the most attractive options for tower CSP plants due to its excellent thermal performance and outstanding pressure-bearing ability. A thorough understanding of thermal and hydraulic performance of supercritical CO_2 in the microchannels at high temperature is the basis for the design and optimization of solar tower receivers in the third generation of CSP plants. In the present study, the heat transfer and flow characteristics of supercritical CO_2 in the microchannels are numerically investigated at relatively wide ranges with inlet temperature of $723\text{--}873 \text{ K}$, heat flux of $100\text{--}500 \text{ kW m}^{-2}$, pressure of $7.5\text{--}30 \text{ MPa}$ and mass flow rate of $0.2\text{--}1.6 \text{ g s}^{-1}$, which cover typical working conditions in solar tower receivers for the third generation of CSP systems. The effects of the microchannel structure and radiation on thermal and hydraulic performance are also discussed. The findings are obtained as follows:

- (1) The inlet and outlet headers of the microchannel are optimized in consideration of good temperature uniformity in the microchannels with relatively low pressure drop.

- (2) Higher mass flow rate obtains poorer thermal performance with larger flow resistance of supercritical CO₂ in the microchannels at high temperature. In addition, the effect of mass flow rate is more pronounced on the average heat transfer coefficient at lower mass flow rate, while it is more on the pressure drop at higher mass flow rate.
- (3) The fluid and wall temperatures, average heat transfer coefficient and pressure drop of supercritical CO₂ in the microchannels all increase nearly linearly with the increases of heat flux and inlet temperature in the high-temperature region.
- (4) High pressure can obtain great hydraulic performance of supercritical CO₂ in the microchannels at high temperature with approximate thermal performance. However, higher pressure requires larger manufacturing cost for the receiver and other equipment for tower CSP plants. Thus, comprehensive consideration is needed to choose the pressure for the solar tower receivers.
- (5) An optimized structure of the multichannel is proposed to improve the uneven flow distribution in the microchannels, which significantly reduces the local high temperature and obtains uniform wall temperature of the microchannels.
- (6) In consideration of the radiation, the effective wall heat flux is smaller than that without radiation, which leads to the lower average heat transfer coefficient and pressure drop in the microchannels. In addition, the effect of the radiation on the thermal performance is more evident than that on hydraulic performance of supercritical CO₂ in the microchannels at high temperature.

Furthermore, the model used in this paper consists of only fluid regions. Solid regions should be included in the model in further study. Based upon the results, high temperatures over 1500 K might exist in the microchannel receivers at high heat flux over 500 kW/m². Thus, the analyses of the thermal stress, thermal shock and material damage are also required. Moreover, another aspect which could be further considered is the effect of non-uniform heat flux distribution on the heat transfer and flow characteristics of supercritical CO₂ in the microchannel receivers.

Author Contributions: Conceptualization, X.Z. and H.G.; methodology, X.Z. and Z.Y.; software and validation, X.Z. and H.L.; formal analysis, X.Z.; investigation, X.Z.; resources and data curation, H.W.; writing—original draft preparation, X.Z.; writing—review and editing, Z.Y.; supervision, H.G.; funding acquisition, X.Z. and H.W. All authors have read and agreed to the published version of the manuscript.

Funding: This research was funded by the Research Foundation of Shenzhen Polytechnic University, grant number 6023312016K; Guangdong Basic and Applied Basic Research Foundation, grant number 2020A1515110257; Post-doctoral Later-stage Foundation Project of Shenzhen Polytechnic University, grant number 6023271010K; Shenzhen Polytechnic High-level Talent Start-up Project Funds, grant number 6021310028K.

Data Availability Statement: No applicable.

Conflicts of Interest: The authors declare no conflict of interest.

References

1. He, Y.L.; Wang, K.; Qiu, Y.; Du, B.C.; Liang, Q.; Du, S. Review of the solar flux distribution in concentrated solar power: Non-uniform features, challenges, and solutions. *Appl. Therm. Eng.* **2019**, *149*, 448–474. [[CrossRef](#)]
2. Shi, H.Y.; Li, M.J.; Wang, W.Q.; Qiu, Y.; Tao, W.Q. Heat transfer and friction of molten salt and supercritical CO₂ flowing in an airfoil channel of a printed circuit heat exchanger. *Int. J. Heat Mass Tran.* **2020**, *50*, 119006. [[CrossRef](#)]
3. Spyridonidou, S.; Vagiona, D.G. A systematic review of site-selection procedures of PV and CSP technologies. *Energy Rep.* **2023**, *9*, 2947–2979. [[CrossRef](#)]
4. Mehos, M.; Turchi, C.; Vidal, J.; Wagner, M.; Ma, Z.; Ho, C.; Kolb, W.; Andraka, C.; Kruiuzenga, A. *Concentrating Solar Power Gen3 Demonstration Roadmap*; No. NREL/TP-5500-67464; National Renewable Energy Lab (NREL): Golden, CO, USA, 2017.
5. Benoit, H.; Spreafico, L.; Gauthier, D.; Flamant, G. Review of heat transfer fluids in tube-receivers used in concentrating solar thermal systems: Properties and heat transfer coefficients. *Renew. Sust. Energ. Rev.* **2016**, *55*, 298–315. [[CrossRef](#)]
6. Sedighi, M.; Padilla, R.V.; Taylor, R.A.; Lake, M.; Izadgoshasb, I.; Rose, A. High-temperature, point-focus, pressurised gas-phase solar receivers: A comprehensive review. *Energy Convers. Manag.* **2019**, *185*, 678–717. [[CrossRef](#)]

7. Qiu, Y.; Li, M.J.; He, Y.L.; Tao, W.Q. Thermal performance analysis of a parabolic trough solar collector using supercritical CO₂ as heat transfer fluid under non-uniform solar flux. *Appl. Therm. Eng.* **2017**, *115*, 1255–1265. [[CrossRef](#)]
8. Khalesi, J.; Sarunac, N. Numerical analysis of flow and conjugate heat transfer for supercritical CO₂ and liquid sodium in square microchannels. *Int. J. Heat Mass Tran.* **2019**, *132*, 1187–1199. [[CrossRef](#)]
9. Liu, K.; Zhao, F.; Jin, Y.; Hu, C.; Ming, Y.; Liu, Y.; Tian, R.; Liu, S. S–CO₂ heat transfer characteristics analysis in PCHE and vertical channel. *Prog. Nucl. Energ.* **2022**, *154*, 104472.
10. Pidaparti, S.R.; Anderson, M.H.; Ranjan, D. Experimental investigation of thermal-hydraulic performance of discontinuous fin printed circuit heat exchangers for supercritical CO₂ power cycles. *Exp. Therm. Fluid Sci.* **2019**, *106*, 119–129. [[CrossRef](#)]
11. Zhang, H.; Shi, L.; Wang, X.; Sun, R.; Yuan, P.; Tian, H.; Shu, G. Heat transfer characteristics of supercritical CO₂ in horizontal rectangular microchannels. *Appl. Therm. Eng.* **2023**, *220*, 119727. [[CrossRef](#)]
12. Wang, K.; Zhang, X.Y.; Zhang, Z.D.; Min, C.H. Three-dimensional shape optimization of fins in a printed circuit recuperator using S-CO₂ as the heat-transfer fluid. *Int. J. Heat Mass Tran.* **2022**, *192*, 122910. [[CrossRef](#)]
13. Roldán, M.I.; Fernández-Reche, J. CFD Analysis of Supercritical CO₂ Used as HTF in a Solar Tower Receiver. In Proceedings of the AIP Conference Proceedings of SOLARPACES 2015: International Conference on Concentrating Solar Power and Chemical Energy Systems, Cape Town, South Africa, 13–16 October 2015.
14. Ho, C.K. Advances in central receivers for concentrating solar applications. *Sol. Energy* **2017**, *152*, 38–56. [[CrossRef](#)]
15. Besarati, S.M.; Yogi Goswami, D.; Stefanakos, E.K. Development of a solar receiver based on compact heat exchanger technology for supercritical carbon dioxide power cycles. *J. Sol. Energy Eng.* **2015**, *137*, 031018. [[CrossRef](#)]
16. Wang, K.; Li, Y.F.; Zhang, Z.D.; Li, S.F.; Fan, Y.H.; Min, C.H. Convective heat transfer characteristics of supercritical CO₂ in mini-channels of compact solar receivers under unilateral heating conditions. *Appl. Therm. Eng.* **2023**, *231*, 120862. [[CrossRef](#)]
17. L'Estrange, T.; Truong, E.; Rymal, C.; Rasouli, E.; Narayanan, V.; Apte, S.; Drost, K. High Flux Microscale Solar Thermal Receiver for Supercritical Carbon Dioxide Cycles. In Proceedings of the ASME 2015 13th International Conference on Nanochannels, Microchannels, San Francisco, CA, USA, 6–9 July 2015.
18. Zada, K.R.; Hyder, M.B.; Kevin Drost, M.; Fronk, B.M. Numbering-up of microscale devices for megawatt-scale supercritical carbon dioxide concentrating solar power receivers. *J. Sol. Energy Eng.* **2016**, *138*, 061007. [[CrossRef](#)]
19. Khivsara, S.D.; Srinivasan, V.; Dutta, P. Radiative heating of supercritical carbon dioxide flowing through tubes. *Appl. Therm. Eng.* **2016**, *109*, 871–877. [[CrossRef](#)]
20. Lemmon, E.W.; Huber, M.L.; McLinden, M.O. *NIST Standard Reference Database 23: Reference Fluid Thermodynamic and Transport Properties-REFPROP*, Version 9.1. Standard Reference Data Program. National Institute of Standards and Technology: Gaithersburg, MD, USA, 2013.
21. Launder, B.E.; Spalding, D.B. *Lectures in Mathematical Models of Turbulence*; Academic Press: London, UK, 1972.
22. Modest, M.F. *Radiative Heat Transfer*; Academic Press: McGraw-Hill, NY, USA, 1993.
23. Kim, D.E.; Kim, M.H. Experimental investigation of heat transfer in vertical upward and downward supercritical CO₂ flow in a circular tube. *Int. J. Heat Fluid Fl.* **2011**, *32*, 176–191. [[CrossRef](#)]
24. Shi, S.; Zhuang, X.; Xu, X. Numerical simulation of convection heat transfer characteristics of supercritical carbon dioxide in a concentrating solar power receiver. *Therm. Power Gener.* **2020**, *49*, 87–92.

Disclaimer/Publisher's Note: The statements, opinions and data contained in all publications are solely those of the individual author(s) and contributor(s) and not of MDPI and/or the editor(s). MDPI and/or the editor(s) disclaim responsibility for any injury to people or property resulting from any ideas, methods, instructions or products referred to in the content.